Supplementary Information for *Topology detection in cavity QED*

Beatriz Pérez-González*, Álvaro Gómez-León, Gloria Platero
*E-mail: bperez03@ucm.es

Appendix A: INPUT-OUTPUT FORMALISM

Using the initial Hamiltonian

Consider the initial Hamiltonian describing a transmission line with two ports, coupled to the topological system via the cavity photons. The total Hamiltonian is:

$$H = \Omega d^{\dagger} d + H_S + g\left(d^{\dagger} + d\right) Z + H_B, \tag{A1}$$

with H_B being the Hamiltonian for the electromagnetic field in the transmission line and its coupling to the cavity,

$$H_B = \sum_{l=1,2} \int_{-\infty}^{\infty} \omega b_l^{\dagger}(\omega)\, b_l(\omega)\, d\omega + i \sum_{l=1,2} \int_{-\infty}^{\infty} \left[\mu_l(\omega)\, b_l^{\dagger}(\omega)\, d - \mu_l(\omega)^*\, d^{\dagger} b_l(\omega)\right] d\omega \tag{A2}$$

where $l = 1, 2$ represent the left/right sides of the cavity, $b_l(\omega)$ is the destruction operator for a photon with energy ω at side l of the cavity and $\mu_l(\omega)$ represents the coupling between the cavity and the outside modes. In this work, we will consider the Markov approximation, which gives $\mu_l(\omega) = \sqrt{\kappa_l/2\pi}$.

Then, the first step is to derive the equation of motion (EoM) for the transmission line photons:

$$\frac{d}{dt} b_l(\nu, t) = -i\nu b_l(\nu, t) + \sqrt{\frac{\kappa_l}{2\pi}}\, d(t) \tag{A3}$$

which can be formally integrated to yield

$$b_l(\nu, t) = b_l(\nu, t_0)\, e^{-i\nu(t-t_0)} + \sqrt{\frac{\kappa_l}{2\pi}} \int_{t_0}^{t} dt' e^{-i\nu\left(t-t'\right)} d(t') \tag{A4}$$

where $t_0 < t$ represents the initial condition. Inserting the previous expression into the EoM for the cavity photons, we get

$$\begin{aligned} \frac{d}{dt} d(t) &= -i\Omega d(t) - igZ(t) - \sum_{l=1,2} \sqrt{\frac{\kappa_l}{2\pi}} \int_{-\infty}^{\infty} d\nu b_l(\nu, t) \\ &= -i\left(\Omega - i\frac{\kappa}{2}\right) d(t) - igZ(t) - \sum_{l=1,2} \sqrt{\kappa_l} b_{in,l}(t) \end{aligned} \tag{A5}$$

where $\kappa = \kappa_1 + \kappa_2$, and we have defined an input field,

$$b_{in,l}\left(t\right) \;=\; \frac{1}{\sqrt{2\pi}}\int_{-\infty}^{\infty} b_l\left(\nu,t_0\right)e^{-i\nu(t-t_0)}d\nu. \tag{A6}$$

Similarly, the solution for $b_l\left(\nu,t\right)$ in (A4) can also be obtained in terms of a final condition $t_1 > t$, which let us define an output field $b_{\mathrm{out},l}\left(t\right)$, fulfilling

$$b_{\mathrm{out},l}\left(t\right) = b_{\mathrm{in},l}\left(t\right) + \sqrt{\kappa_l}d\left(t\right) \tag{A7}$$

One has to solve the EoM for $Z\left(t\right)$ as well. We consider the basis of eigenstates of the fermionic Hamiltonian

$$H_S = \sum_{\alpha=1}^{N} E_\alpha X^{\alpha,\alpha},\; Z = \sum_{\vec{\alpha}} Z_{\vec{\alpha}} X^{\vec{\alpha}} \tag{A8}$$

with $X^{\vec{\alpha}} = X^{\alpha_1,\alpha_2} = |\alpha_1\rangle\langle\alpha_2|$, and calculate the equation of motion for an arbitrary Hubbard operator $X^{\vec{\alpha}}$

$$\partial_t \tilde{X}^{\vec{\alpha}}(t) = i\left(\tilde{E}_{\vec{\alpha}} - i\frac{\gamma}{2}\right)\tilde{X}^{\vec{\alpha}}(t) + ig\left(d^\dagger(t)+d(t)\right)\sum_\beta\left(\tilde{Z}_{\beta,\alpha_1}\tilde{X}^{\beta,\alpha_2}(t) - \tilde{Z}_{\alpha_2,\beta}\tilde{X}^{\alpha_1,\beta}(t)\right), \tag{A9}$$

where $E_{\vec{\alpha}} = E_{\alpha_1} - E_{\alpha_2}$ and we have also included the phenomenological spectral broadening factor $\gamma/2$. The product $d^{(\dagger)}\left(t\right)X\left(t\right)$ can be decomposed as

$$d^{(\dagger)}\left(t\right)X\left(t\right) \approx \langle X\rangle d^{(\dagger)}\left(t\right) + \langle d^{(\dagger)}\rangle X(t), \tag{A10}$$

where we are neglecting any terms accounting for correlation between operators, which is a valid approach in the small-g regime. Under this condition, one can safely calculate $\langle X\rangle$ and $\langle d^{(\dagger)}\rangle$ using the corresponding unperturbed Hamiltonians, H_S and $\Omega d^\dagger d$, respectively. Then, one can easily see that $\langle d^{(\dagger)}\rangle = 0$, and hence the solution for the EoM in (A9) in frequency space reads

$$X^{\vec{\alpha}}\left(\omega\right) \simeq gd\left(\omega\right)\frac{\sum_\beta\left(Z_{\alpha_2,\beta}\langle X^{\alpha_1,\beta}\rangle - Z_{\beta,\alpha_1}\langle X^{\beta,\alpha_2}\rangle\right)}{\omega + E_{\vec{\alpha}} - i\frac{\gamma}{2}}. \tag{A11}$$

We have also neglected the contribution of $\langle X\rangle d^\dagger\left(\omega\right)$, as typically done in the literature [1]. Substituting this result in (A5), we find

$$d\left(\omega\right) = \frac{i\sum_{l=1,2}\sqrt{\kappa_l}b_{\mathrm{in},l}\left(\omega\right)}{\Omega - \omega - i\frac{\kappa}{2} + g^2\chi\left(\omega\right)} \tag{A12}$$

where

$$\chi\left(\omega\right) = \sum_{\vec{\alpha},\beta}\frac{Z_{\vec{\alpha}}\left(Z_{\alpha_2,\beta}\langle X^{\alpha_1,\beta}\rangle - Z_{\beta,\alpha_1}\langle X^{\beta,\alpha_2}\rangle\right)}{\omega + E_{\vec{\alpha}} - i\frac{\gamma}{2}}. \tag{A13}$$

Using (A7), and taking into account that the input is inserted through the left port ($l = 1$) into the cavity, and the output is collected through the right one ($l = 2$), we can write the transmission as

$$t_c(\omega) = \frac{\langle b_{\text{out},2}\rangle}{\langle b_{\text{in},1}\rangle} = \frac{i\sqrt{\kappa_1\kappa_2}}{\Omega - \omega - i\frac{\kappa}{2} + g^2\chi(\omega)} \tag{A14}$$

which is the usual result for the cavity transmission, with $\chi(\omega)$ being the electronic susceptibility.

Using the mean-field Hamiltonian

If we instead consider the MF Hamiltonian for the cavity, topological system and their interaction, we start from the following expression

$$\begin{aligned} H &= \Omega d^\dagger d - \frac{g^2\langle Z\rangle^2}{\Omega} + \tilde{H}_{\text{MF},S} + g\left(d^\dagger + d\right)\tilde{Z} \\ &+ \sum_{l=1,2}\int_{-\infty}^{\infty} \omega b_l^\dagger(\omega) b_l(\omega) d\omega \\ &+ i\sum_{l=1,2}\sqrt{\frac{\gamma_l}{2\pi}}\int_{-\infty}^{\infty} d\omega \left[b_l^\dagger(\omega)\left(d - \frac{g\langle Z\rangle}{\Omega}\right) - \left(d^\dagger - \frac{g\langle Z\rangle}{\Omega}\right) b_l(\omega)\right] \end{aligned} \tag{A15}$$

where $\tilde{Z} = Z - \langle Z\rangle$ and $\tilde{H}_{\text{MF},S} = H_{\text{MF},S} - \frac{2g^2\langle Z\rangle}{\Omega} Z$. Note that the cavity operators have been rotated to $\tilde{d}^{(\dagger)} = d^{(\dagger)} - \frac{g\langle Z\rangle}{\Omega}$ in order to diagonalize their MF Hamiltonian. The self-consistent values of $\langle Z\rangle$ and $\langle d^{(\dagger)}\rangle$ have been determined ignoring the coupling to the transmission line, as explained in the main text. Importantly, the cavity operators in H_B have also been rotated accordingly. This time, the EoM for $b_l(\nu, t)$ yields the following solution

$$\tilde{b}_l(\nu, t) = b_l(\nu, t) - \frac{g\langle Z\rangle}{\Omega}\sqrt{\frac{\kappa_l}{2\pi}}\frac{1 - e^{-i\nu(t-t_0)}}{i\nu} \tag{A16}$$

Compared to (A4), we have an extra term due to the rotation of the bosonic operators, that depends on the state of the fermionic system through $\langle Z\rangle$. The EoM for $d(t)$ has the same form, with redefined input and output fields

$$\tilde{b}_{\text{in},l}(t) = b_{\text{in},l}(t) - \frac{g\sqrt{\kappa_l}\langle Z\rangle}{2\pi\Omega}\int_{-\infty}^{\infty}\frac{1 - e^{-i\nu(t-t_0)}}{i\nu} d\nu, \tag{A17}$$

$$\tilde{b}_{\text{out},l}(t) = b_{\text{out},l}(t) + \frac{g\sqrt{\kappa_l}\langle Z\rangle}{2\pi\Omega}\int_{-\infty}^{\infty}\frac{1 - e^{i\nu(t_1-t)}}{i\nu} d\nu, \tag{A18}$$

also fullfilling that $\tilde{b}_{\text{out},l}(t) = \tilde{b}_{\text{in},l}(t) + \sqrt{\kappa_l} d(t)$. On the other hand, the Hubbard operators change as well due to the presence of the extra MF contribution in the fermionic Hamiltonian

$$\tilde{H}_S = H_S - \frac{2g^2\langle Z\rangle}{\Omega} Z = \sum_{\alpha=1}^{N} \tilde{E}_\alpha \tilde{X}^{\alpha,\alpha}, \tag{A19}$$

$$\tilde{Z} = \sum_{\vec{\alpha}} \tilde{Z}_{\vec{\alpha}} \tilde{X}^{\vec{\alpha}}. \tag{A20}$$

The EoM for $\tilde{X}$ has the same form of (A9), but substituting the eigenvalues and eigenvectors of the unperturbed fermionic Hamiltonian H_S by the ones of MF Hamiltonian $\tilde{H}_S$. To solve the EoM, we take fluctuations to be small, which is a valid assumption when g is both small and very large, i.e., when the MF Hamiltonian $\tilde{H}_S + \tilde{H}_\Omega$ accurately describes the physics of the system, without considering the fluctuations Hamiltonian $\tilde{H}_\delta$. Under this condition, we can write $d^{(\dagger)}(t)\,\tilde{X}(t) \approx \langle\tilde{X}\rangle d^{(\dagger)}(t) + \langle d^{(\dagger)}\rangle\tilde{X}(t)$. Again, we neglect any correlation created by the fluctuations Hamiltonian, which acts as an effective interaction between the two MF Hamiltonians. Note that $\langle d^{(\dagger)}\rangle = 0$ when evaluated using the MF photonic Hamiltonian in the rotated frame, $\tilde{H}_\Omega$.
Formally, the decoupling employed to solve (A20) is the same as the one used in (A9). Then, the solution for $\tilde{X}$ gives

$$\tilde{X}^{\vec{\alpha}}(\omega) \simeq g d(\omega)\,\frac{\sum_\beta\left(\tilde{Z}_{\alpha_2,\beta}\langle\tilde{X}^{\alpha_1,\beta}\rangle - \tilde{Z}_{\beta,\alpha_1}\langle\tilde{X}^{\beta,\alpha_2}\rangle\right)}{\omega + \tilde{E}_{\vec{\alpha}} - i\frac{\gamma}{2}}. \tag{A21}$$

Note that (A13) is analogous to (A21), but all parameters have been renormalized due to MF. Finally, the transmission can be written as

$$t_c(\omega) = \frac{i\sqrt{\kappa_1\kappa_2}}{\Omega - \omega - i\frac{\kappa}{2} + g^2\tilde{\chi}(\omega)}. \tag{A22}$$

where now $\tilde{\chi}(\omega)$ is the susceptibility written in terms of the MF Hamiltonian.

Appendix B: TRANSMISSION AND PHOTONIC GREEN'S FUNCTION

The starting point is the EoM for the photonic operator $d(t)$ (A5) in Fourier space

$$i\omega d(\omega) = -i\left(\Omega - i\frac{\kappa}{2}\right)d(\omega) - ig\sum_{\vec{\alpha}} Z_{\vec{\alpha}}\tilde{X}^{\vec{\alpha}}(\omega) - \sum_{l=1,2}\sqrt{\kappa_l}\tilde{b}_{\mathrm{in},l}(\omega) \tag{B1}$$

The losses of the cavity have been included through the phenomenological factor κ. This equation depends on $\tilde{X}^{\vec{\alpha}}(\omega)$, which has its own dynamics as well,

$$\begin{aligned} i\omega\tilde{X}^{ij}(\omega) \;=\; & -i\left(\tilde{E}_j - \tilde{E}_i + i\frac{\gamma}{2}\right)\tilde{X}^{ij}(\omega) \\ & -ig\left(d^\dagger(\omega) + d(\omega)\right)\sum_m\left(Z_{jm}\tilde{X}^{im}(\omega) - Z_{mi}\tilde{X}^{mj}(\omega)\right). \end{aligned} \tag{B2}$$

Solving this equation implies writting the EoM for $d^{(\dagger)}\tilde{X}^{ij}$, which at the same time is coupled to higher-order operators. Then, we can write an infinite vector with all the relevant operators involved, $\vec{v} = \left(d, X^{ij}, ...\right)$, and the system of equations turns out to be

$$(\omega - A)\,\vec{v} = \vec{v}_0 \tag{B3}$$

where A is the coefficients matrix and $\vec{v}_0$ represents the inhomogeneous term.

Then, on the other hand, we can write the EoM for the retarded photonic Green function, defined as $G(t) = -i\theta(t)\langle\left[d(t), d^\dagger\right]\rangle \equiv \langle\langle d(t); d^\dagger\rangle\rangle_t$, yielding

$$\omega G(\omega) = 1 + \left(\Omega - i\frac{\kappa}{2}\right)\tilde{G}(\omega) + g\sum_{ij} M_{ij}(\omega) \tag{B4}$$

where $\tilde{M}_{ij}(\omega) = \langle\langle X^{ij}; a^\dagger\rangle\rangle_\omega$. Note that the dissipative factor enters the EoM for $G(\omega)$ through the integration of the external modes and their coupling to the cavity photons, just as in Eq. A5. Again, this EoM is coupled to higher-order Green functions, resulting in an infinite system of coupled differential equations. In matrix form, we have

$$(\omega - A')\,\vec{V}(\omega) = \vec{V}_0 \tag{B5}$$

where $\vec{V} = (G, M_{ij}, ...)$ and $\vec{V}_0$ is the inhomogeneous term by comparison. One can see that $A = A'$, which indicates that $G(\omega) = -i\theta(t)\langle\left[a(t), a^\dagger\right]\rangle$ is the resolvent of (B1).

Finally, we can compare the first component of each system of equations, namely $a(\omega) = -i(\omega - H)^{-1}\sum_{l=1,2}\sqrt{\kappa_l}\tilde{b}_{\mathrm{in},l}(\omega)$ and $G(\omega) = (\omega - H)^{-1}$, and see that

$$a(\omega) = -iG(\omega)\sum_{l=1,2}\sqrt{\kappa_l}\tilde{b}_{\mathrm{in},l}(\omega). \tag{B6}$$

The last step is to write the transmission as a function of $a(\omega)$, knowing that $\tilde{b}_{\mathrm{out,l}}(t) = \tilde{b}_{\mathrm{in,l}}(\omega) + \sqrt{\kappa_l}a(\omega)$ and that the only input is through port 1

$$t_c = \frac{\langle\tilde{b}_{\mathrm{out},2}\rangle}{\langle\tilde{b}_{in,1}\rangle} = \frac{\langle\tilde{b}_{\mathrm{in},2}\rangle + \sqrt{\kappa_2}\langle a\rangle}{\langle\tilde{b}_{in,1}\rangle} = -i\sqrt{\kappa_2}\sqrt{\kappa_1}G(\omega). \tag{B7}$$

It is very enlightening to obtain an analytical expression for the photonic Green function in the case of $g \ll \Omega, \tilde{E}_{\vec{\alpha}}$ and $g \gg \Omega, \tilde{E}_{\vec{\alpha}}$. The equation of motion of $G(\omega)$ (Eq. B4) is coupled to the mixed Green function $\tilde{M}_{ij}$, which gives

$$\begin{aligned}\omega\tilde{M}_{ij} &= (\tilde{E}_j - \tilde{E}_i)\tilde{M}_{ij} + \sum_l Z_{jl}\langle\langle(d^\dagger + d)\tilde{X}^{il}; d^\dagger\rangle\rangle_\omega \\ &\quad - \sum_l Z_{li}\langle\langle(d^\dagger + d)\tilde{X}^{lj}; d^\dagger\rangle\rangle\end{aligned} \tag{B8}$$

Note the presence of the higher-order Green function $\langle\langle(d^\dagger + d)\tilde{X}; d^\dagger\rangle\rangle$. Fluctuations are negligible in the small and very-large coupling regimes, which let us employ the following decoupling scheme

$$\langle\langle(d^\dagger + d)\tilde{X}; d^\dagger\rangle\rangle \approx \big(\langle d^\dagger\rangle + \langle d\rangle\big)\langle\langle\tilde{X}; d^\dagger\rangle\rangle_\omega + \langle\tilde{X}\rangle\langle\langle d; d^\dagger\rangle\rangle_\omega \tag{B9}$$

This approximation is analogous to the decoupling scheme $d^{(\dagger)}(t)\,\tilde{X}(t) \approx \langle\tilde{X}\rangle d^{(\dagger)}(t) + \langle d^{(\dagger)}\rangle\tilde{X}(t)$ presented in the main text used to solve the EoM for the photonic operator. Again, it implies that we are neglecting first-order correlations between fermionic and photonic operators, and under this assumption the system of equations including Eqs. B4 and B8 can be closed and solved, obtaining

$$G(\omega) = -\frac{1}{\Omega - \omega + g^2\tilde{\chi}(\omega)}. \tag{B10}$$

for the photonic Green function. It is straight-forward to see that the previous expression verifies the relation between the transmission and $G(\omega)$ presented in Eq. 13 in the main text, when compared with Eq. 10 in the limits of $g \ll \Omega, \tilde{E}_{\vec{\alpha}}$ and $g \gg \Omega, \tilde{E}_{\vec{\alpha}}$. Note that the phenomenological factors have to be added as well.

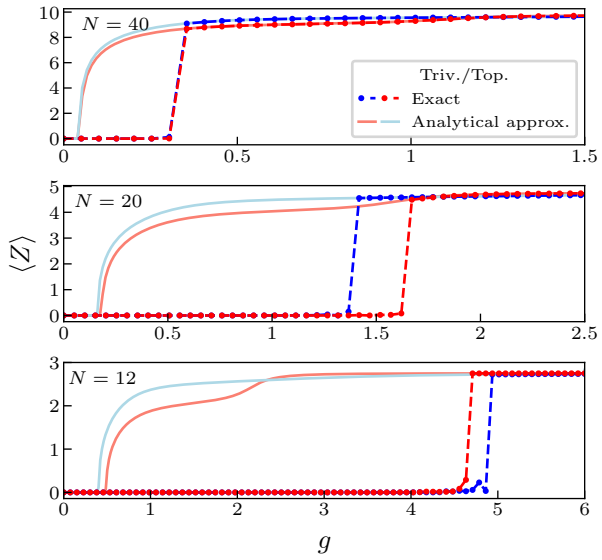

Figure SM1: **$\langle \mathbf{Z} \rangle$ for different N**. $\langle Z \rangle$ as a function of the coupling constant g for $\Omega = 10$, $\delta = \pm 0.6$ (trivial/topological phase) and different system sizes: $N = 40$ (top), $N = 20$ (middle), $N = 12$ (bottom). The value of $\langle Z \rangle$ has been calculated self-consistently using the MF Hamiltonian (solid) and exact diagonalization (dashed-dotted line). The chain size modifies the value of the critical point at which the system polarizes, enhancing or reducing the difference between topological phases at the phase transition

Appendix C: SOLUTION FOR $\langle Z \rangle$

In this section we compare the solution of $\langle N \rangle$ for different system sizes N. Fig. SM1 shows $\langle Z \rangle$ as a function of g for the MF case and the exact one, as in the main text, but including different chain lengths: $N = 12$, 20 and 40. The main features that are commented on the main text are still present; however, we can see that changes in N modify the critical value at which the system polarizes, enhancing or reducing the difference between topological phase at the transition, as well as the final value in the limit $g \to \infty$. Also, as the number of sites N increases, the critical value of g at which the phase transition happens is reduced (see Fig. SM1). This is expected, since the effective strength of the coupling at each site $g_i = gx_i$ gets larger as more sites are considered.

Appendix D: TOPOLOGICAL DETECTION IN THE SMALL COUPLING REGIME OCCUPYING AN EDGE STATE

We have shown that the cavity transmission cannot act as a topological marker if the lowest-energy state is occupied. On the contrary, if the edge state is initially occupied in the topological phase, the transmission peak at $\omega = \Omega$ should remain unaffected by the interaction, as opposed to the behaviour of the trivial phase, in which changes in t_c are expected. This assymetry between phases can be maximized if the cavity frequency Ω is resonant with an electronic transition $E_{\vec{\alpha}}$ (eigenenergy of the unperturbed fermionic Hamiltonian H_S) and in particular, with the gap of the chain. While the transmission for the non-trivial topological phase does not change compared to the uncoupled cavity transmission (the bulk states are decoupled from the edge states), the presence of a direct resonance in the trivial phase results in a Rabi splitting: the peak of maximum transmission divides into two distinct modes, separated by the Rabi frequency Ω_r [2], which is often detected in experiments and indicates that the regime $g > \{\kappa, \gamma\}$ is achieved [3–7].

This is shown in Fig. SM2. We consider the top state in the valence band is occupied for the trivial phase, while the edge state is occupied for the topological phase. This choice is motivated by the fact that both states are adiabatically connected across the topological phase transition, as δ is varied from negative to positive values. While the decoupling between bulk and edge states explains the absence of any changes in t_c for the topological phase, a Rabi splitting appears for the trivial phase. The analytical approximation captures the position of each peak in ω (as indicated by the

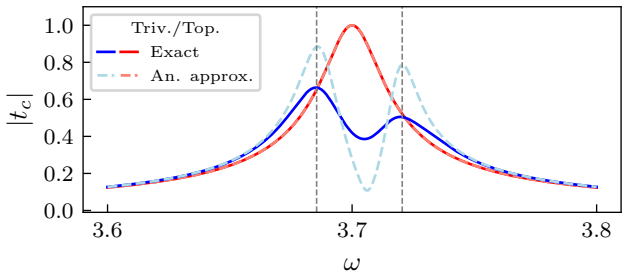

Figure SM2: $|\mathbf{t_c}(\omega)|$ **as a function of** ω. Dashed lines indicate the analytical approximation (Eq. 13), while solid lines correspond to the exact solution (Eq. 10). We consider the $(N/2)$-th state occupied, corresponding to the edge state in the topological phase and the top of the valence band in the trivial phase. The parameters used are: $\Omega = 3.7$, $g = 0.06$, $\delta = \pm 0.925$ (trivial/topological phase, in blue/red, respectively), $N = 20$, $\gamma = \kappa_1 = \kappa_2 = 0.01$.

dashed, grey vertical lines), as well as their relative height, though the exact shape of the peaks is not reproduced. This disagreement can be explained by correlated excitations that strongly modify the system due to resonant conditions.

In conclusion, for the small-g regime it is important to stress that detection of the topological phase requires the system to be initialized in an edge state. Otherwise the cavity transmission cannot differentiate between the two phases. One disadvantage of this regime of operation is that the measurement needs to be carried out before thermalization happens, but this could be avoided by filling the fermionic system to half-filling (however, in this case many systems require to account for particle interactions as well).

Appendix E: SCHRIEFFER-WOLFF TRANSFORMATION

We begin with the Hamiltonian $H = \tilde{H}_S + \tilde{H}_\Omega + \tilde{H}_\delta$, as defined in the main text, written in the basis of eigenstates of $\tilde{H}_S$:

$$H = \sum_i \tilde{E}_\alpha \tilde{X}^{\alpha,\alpha} + \Omega d^\dagger d - \frac{g^2 \langle Z \rangle}{\Omega} + g(d^\dagger + d)\tilde{Z} \tag{E1}$$

We propose the following ansatz for the generator S of the Schrieffer-Wolff (S-W) transformation,

$$S = \sum_{\vec{\alpha}} \left(\Gamma^+_{\vec{\alpha}} d^\dagger + \Gamma^-_{\vec{\alpha}} d\right) \tilde{X}^{\vec{\alpha}} \tag{E2}$$

where $\vec{\alpha} = (\alpha_1, \alpha_2)$. Imposing $\tilde{H}_\delta = -[S, \tilde{H}_S + \tilde{H}_\Omega]$, one finds the following equations for the free parameters:

$$\Gamma^\pm_{\vec{\alpha}} = \frac{g\tilde{Z}_{\vec{\alpha}}}{\tilde{E}_{\vec{\alpha}} \pm \Omega}. \tag{E3}$$

with $\tilde{E}_{\vec{\alpha}} = \tilde{E}_{\alpha_1} - \tilde{E}_{\alpha_2}$. This results in the final form of the transformation:

$$S = g(d^\dagger + d) \sum_{\vec{\alpha}} \frac{\tilde{E}_{\vec{\alpha}} \tilde{Z}_{\vec{\alpha}}}{\tilde{E}^2_{\vec{\alpha}} - \Omega^2} - g\Omega(d^\dagger - d) \sum_{ij} \frac{\tilde{Z}_{\vec{\alpha}}}{\tilde{E}^2_{\vec{\alpha}} - \Omega^2} \tilde{X}^{\vec{\alpha}} \tag{E4}$$

The correction to the Hamiltonian is proportional to:

$$\left[S,\tilde{H}_\delta\right]=g^2(d^\dagger+d)^2\sum_{\vec{\alpha}}\frac{\tilde{E}_{\vec{\alpha}}\tilde{Z}_{\vec{\alpha}}}{\tilde{E}^2_{\vec{\alpha}}-\Omega^2}Y^-_{\vec{\alpha}}-g^2\Omega(d^{\dagger 2}-d^2)\sum_{\vec{\alpha}}\frac{\tilde{Z}_{\vec{\alpha}}}{\tilde{E}^2_{\vec{\alpha}}-\Omega^2}Y^-_{\vec{\alpha}}+g^2\Omega\sum_{\vec{\alpha}}\frac{\tilde{Z}_{\vec{\alpha}}}{\tilde{E}^2_{\vec{\alpha}}-\Omega^2}Y^+_{\vec{\alpha}} \tag{E5}$$

with

$$Y^\pm_{\vec{\alpha}}=\sum_\beta(\tilde{Z}_{\alpha_2\beta}\tilde{X}^{\alpha_1\beta}\pm\tilde{Z}_{\beta\alpha_1}X^{\beta\alpha_2}) \tag{E6}$$

Finally, one can write the effective Hamiltonian up to second order, neglecting two-photon processes and constant terms,

$$\begin{aligned}\bar{H}\simeq\tilde{H}_S+\Omega d^\dagger d+\frac{1}{2}[S,\tilde{H}_\delta] \;=\; &\sum_\alpha\tilde{E}_\alpha\tilde{X}^{\alpha,\alpha}+\frac{g^2}{2}\sum_{\vec{\alpha}}\tilde{Z}_{\vec{\alpha}}\left[\frac{\sum_\beta\tilde{Z}_{\alpha_2\beta}\tilde{X}^{\alpha_1\beta}}{\tilde{E}_{\vec{\alpha}}-\Omega}-\frac{\sum_n\tilde{Z}_{\beta\alpha_1}\tilde{X}^{\beta\alpha_2}}{\tilde{E}_{\vec{\alpha}}+\Omega}\right]\\&+\left[\Omega+g^2\sum_{\vec{\alpha}}\tilde{\Omega}_{\vec{\alpha}}\tilde{Y}^-_{\vec{\alpha}}\right]d^\dagger d.\end{aligned} \tag{E7}$$

where $\tilde{\Omega}_{\vec{\alpha}}$ is defined in the main text.

Appendix F: ENTANGLEMENT ENTROPY AND ENERGY SPECTRUM

As shown in Fig. 5(c) in the main text, there is a $\log(2)$-plateau in the topological phase for small-g when the $N/2$-th state is occupied, corresponding to one of the topological edge states. Its drop at $g\sim 0.84$ corresponds with its anti-crossing with a state belonging to the bulk bands and indicates the destruction of maximal entanglement for the $N/2$-th state.

However, the topological contribution to the entanglement entropy is not lost at this point, but migrates from one state to the other as they further anti-cross in the energy spectrum. Figure SM3 shows a zoom of the energy spectrum where the edge states penetrate into the bulk bands, together with the entanglement entropy S_A associated to the occupation of each of them. For small-g, the $\log(2)$ plateau corresponds to the $N/2$-th (red) and $(N/2+1)$-th (light brown) states (edge states), while the rest of them are not maximally entangled (their S_A depends on the partition used). The first anti-crossing encountered in the spectrum (at $g\sim 0.78$) between the light brown and blue (top state in the valence band) states, corresponds to the appearance of a $\log(2)$-plateau for the later, while the entanglement between the ending sites is lost for the edge state.

On the other hand, as g is increased, the $N/2$-th state anti-crosses with other states as well. Figure SM4 shows that each of these anti-crossings correspond to the abrupt changes in S_A obtained for the $N/2$-th state (Fig. 5(c)), by zooming into the first four of them.

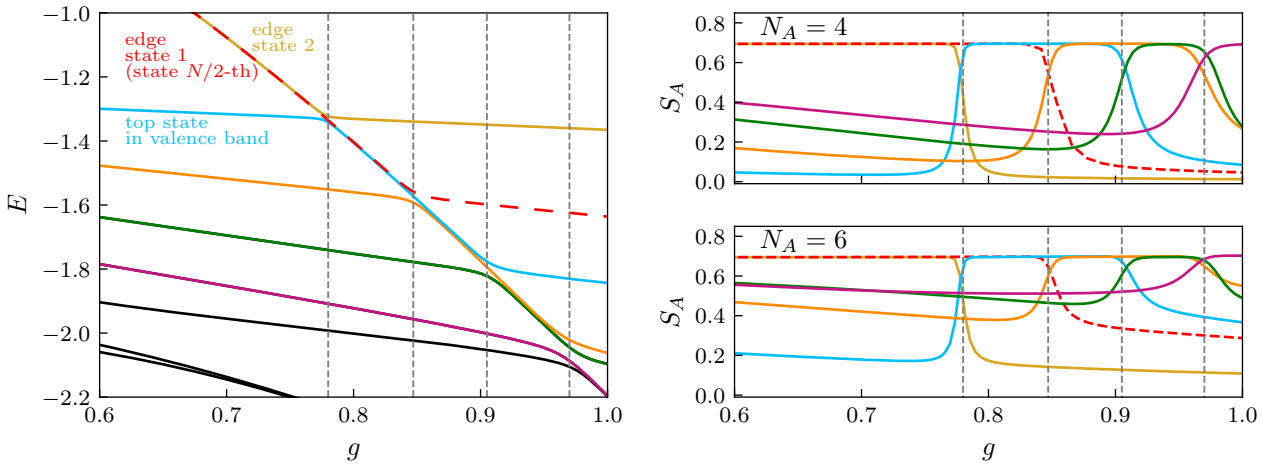

Figure SM3: **Entanglement entropy and the energy spectrum**. Left plot: zoom into the energy spectrum, as a function of g, corresponding to the anti-crossing (dashed, grey vertical lines) of energy states triggered by the entrance of the edge states into the bulk band. The parameters chosen are: $\Omega = 10$ $\delta = -0.6$, $N = 20$. Each state is depicted in a different color: light brown for the $\left(\frac{N}{2}+1\right)$ -th state, red for the $N/2$-th (corresponding to the two edge states), blue for the $\left(\frac{N}{2}-1\right)$-th (top state in the valence band), orange for the $\left(\frac{N}{2}-2\right)$-th, green for the $\left(\frac{N}{2}-3\right)$-th and violet for the $\left(\frac{N}{2}-4\right)$-th (the following states appear in black). The first anti-crossing at $g \sim 0.78$ happens between the edge state (light brown) and the top state in the valence band (blue). The second anti-crossing at $g \sim 0.9$ happens between the edge state (red) and $\left(\frac{N}{2}-2\right)$-th state in the bulk band (orange). For higher values of the coupling constant (only shown up to $g = 1$), sucessive anti-crossings between adjacent states appear. Right plot: entanglement entropy for each state (same color code as in the left plot), for different partitions $N = 4$ (upper plot) and $N = 6$ (lower plot). For small-g, the $\log(2)$ plateau corresponds to the $N/2$-th state, while the rest of them are not maximally entangled (their S_A depends on the partition used). Each time a state from the bulk band anti-crosses with an edge state, it turns into an edge state itself, so that the $\log(2)$ plateau (originally caused by the non-trivial topology of the fermionic system) migrates from one state to the other.

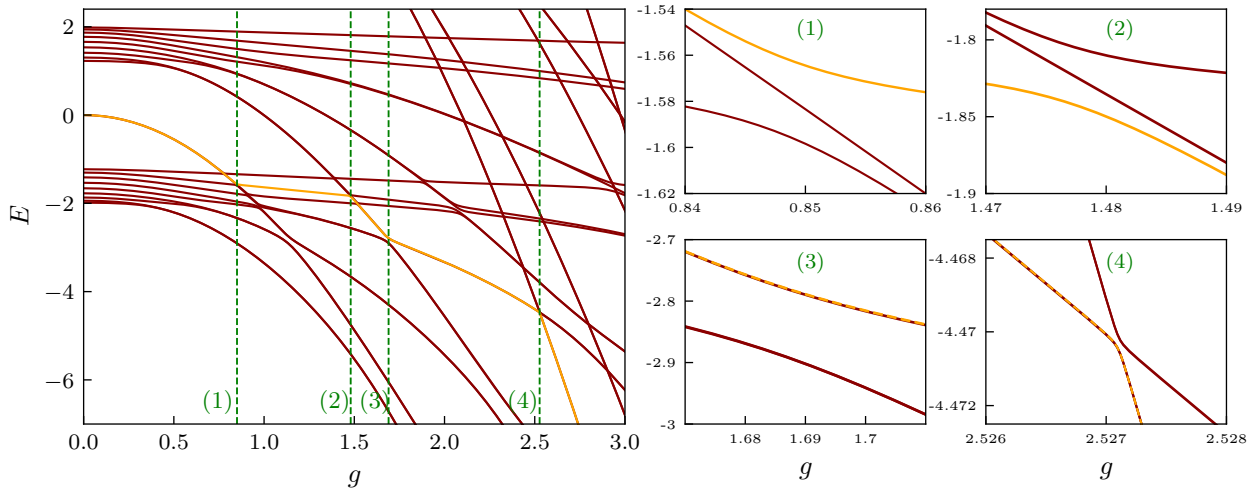

Figure SM4: **Anti-crossings for the N/2$^{\text{th}}$ state in the topological phase.** Left plot: energy spectrum for the zero-photon band as a function of g. The $N/2$-th state (for which the entanglement entropy is calculated in Fig. 6(c)) is represented in orange. The green, dashed lines represent the first four anti-crossings for this state, which correspond to the first four abrupt changes in S_A in Fig. 6(c). Right plots: zoom into the first four anti-crossings of the $N/2$-th state.

[1] S. Kohler, Phys. Rev. A **98**, 023849 (2018), URL https://link.aps.org/doi/10.1103/PhysRevA.98.023849.
[2] D. F. Walls and G. J. Milburn, *Quantum Optics* (Springer, 2008).
[3] A. J. Landig, J. V. Koski, P. Scalino, U. C. Mendes, A. Blais, C. Reichl, W. Wegscheider, A. Wallraff, K. Ensslin, and T. Ihn, Nature **560**, 179 (2018).
[4] A. Stockklauser, P. Scarlino, J. V. Koski, S. Gasparinetti, C. K. Andersen, C. Reichl, W. Wegscheider, T. Ihn, K. Ensslin, and A. Wallraff, Phys. Rev. X **7**, 011030 (2017), URL https://link.aps.org/doi/10.1103/PhysRevX.7.011030.
[5] X. Mi, M. Benito, S. Putz, D. M. Zajac, J. M. Taylor, G. Burkard, and J. R. Petta, Nature **555**, 590 (2018).
[6] N. Samkharadze, G. Zheng, N. Kalhor, D. Brousse, A. Sammak, U. C. Mendes, A. Blais, G. Scappucci, and L. M. K. Vandersypen, Science **359**, 1123 (2018).
[7] X. Mi, J. M. Cady, D. M. Zajac, P. W. Deelman, and J. R. Petta, Science **355** (2017).